Energy Storage Materials 15 (2018) 380–387

Contents lists available at ScienceDirect

Energy Storage Materials

journal homepage: www.elsevier.com/locate/ensm

Solid solution nitride/carbon nanotube hybrids enhance electrocatalysis of oxygen in zinc-air batteries

Guanjie He[a,b], Xiaoyu Han[a], Benjamin Moss[c], Zhe Weng[b], Srinivas Gadipelli[a], Feili Lai[e], Andreas G. Kafizas[c], Daniel J.L. Brett[d], Zheng Xiao Guo[a,*], Hailiang Wang[b], Ivan P. Parkin[a,*]

[a] Christopher Ingold Laboratory, Department of Chemistry, University College London, 20 Gordon Street, London WC1H 0AJ, UK
[b] Department of Chemistry and Energy Sciences Institute, Yale University, 810 West Campus Drive, West Haven, CT 06516, USA
[c] Department of Chemistry, Imperial College London, South Kensington Campus, London SW7 2AZ, UK
[d] Electrochemical Innovation Lab, Department Chemical Engineering, University College London, London WC1E 7JE, UK
[e] State Key Laboratory of Molecular Engineering of Polymers, Department of Macromolecular Science, Fudan University, Shanghai 200433, China

ARTICLE INFO

Keywords:
Solid solution nitride
Electrocatalyst
Zn-air battery
Computational simulation

ABSTRACT

Bi-functional electrocatalysts capable of both the oxygen reduction reaction (ORR) and the oxygen evolution reaction (OER) are highly desirable for a variety of renewable energy storage and conversion technologies. To develop noble metal alternatives for catalysis, non-noble metal compounds have been tremendously pursued but remain non-ideal to issues relating to stability and population of the number of exposed active sites. Inspired by Engel-Brewer valence bond theory, strongly coupled nickel-cobalt-nitride solid-solution/carbon nanotube hybrids were developed by tuning their bifunctionalities from an atomistic scale. The as-synthesized catalysts demonstrate superior catalytic properties to commercial noble-metal based counterparts, *i.e.* platinum on a carbon support for ORR and iridium oxide for OER, also with much enhanced stability. First-principle calculations and structural analysis show that the optimized structures potentially possess multiple active sites, both bulk-surface response and separated surface charge distribution from optimization of Ni/Co nitrides could contribute to synergistic effects for improved catalytic performances. This study provides not only unique theoretical insights but also a design concept for producing effective bi-functional catalysts with balanced-ORR/OER active sites for this class of transition metal nitride hybrid system and paves the way for exploring other metal nitrides for similar purposes.

Increasing demands for renewable energy have stimulated the rapid development in the generation of novel energy storage and conversion technologies [1,2]. The oxygen reduction and/or evolution reactions (ORR/OER, respectively) are central to the efficiency of a wide range of energy conversion applications, such as metal-air batteries, reversible fuel cells and water splitting devices [3–6]. Despite considerable efforts in the development of new catalysts, the commercial platinum/carbon for ORR and iridium oxide for OER, remain the benchmark materials [7,8]. However, these noble metal based catalysts suffer from high cost, poor catalytic reversibility and unsatisfactory long-term stability [9]. Overall, the ORR and OER are reversible reactions but commonly used electrocatalysts do not service both reactions well [10,11]. Hence, it is of great importance to design and develop economical, effective and stable bi-functional oxygen electrocatalysts to reduce the potential gap between these two sluggish processes using a single electrode formulation.

Besides noble metals, transition metal-based materials and doped carbon structures have been explored for bi-functional oxygen electrocatalysis [10,12–18]. First-row transition metals with cost-effectiveness and abundance have attracted intensive attention for such applications due to their incompletely filled d-orbitals offering a rich range of possible oxidation states, which accommodates the catalytic performance. Previous studies show that nickel, cobalt, manganese and iron-based hydroxides/oxides have been shown promising ORR and/or OER properties [4,10,13,14,17,19–21]. However, their intrinsically poor electron conductivities and the limited number of active sites impede their electrocatalytic performance.

Based on the Engel-Brewer valence bond theory, early transition metal carbides and nitrides could increase the effective s-p electron count of metals [22], and thus, the structures and chemical properties of the Group VIII metal carbides and nitrides often resemble those of noble metals. In 1973, Levy and Boudart were first to discover that tungsten carbide has platinum-like behaviour in surface catalysis [23]. Recently, the electrocatalytic properties of transition metal nitrides have been intensively investigated. Nickel nitride nanosheets were

* Corresponding authors.
E-mail addresses: z.x.guo@ucl.ac.uk (Z.X. Guo), hailiang.wang@yale.edu (H. Wang), i.p.parkin@ucl.ac.uk (I.P. Parkin).

https://doi.org/10.1016/j.ensm.2018.08.020
Received 18 May 2018; Received in revised form 11 August 2018; Accepted 23 August 2018
Available online 24 August 2018

designed by Xie et al. and showed excellent OER properties, with a smaller Tafel slope of 45 mV/dec compared to the oxide counterparts [24]. Based on both experimental and theoretical approaches, these nitride ultrathin nanosheets have been shown to exhibit metallic electroconductivity. Moreover, binary transition metal compounds offer diversity and tunability for electrocatalysis. From our previous work, the ORR performance of binary nickel and cobalt sulphides could be tuned on an atomistic perspective [25]. However, the reported bi-transition metal compounds, such as $NiCo_2S_4$ and Ni_3FeN, could lose their catalytic activity due to decreased electrical conductivity, reduced active sites or structural corruption in alkaline aqueous electrolytes [5,19,25–27]. Hence, improvements in materials design is critical for both highly active and stable bi-functional electrocatalysts. In addition, a better understanding of the active catalytic sites and the structrual/electronic evolution within a series of solid solution nitrides have not been studied until now, and sheds a unique light on the rational design of transition metal nitride catalysts.

In this work, Ni/Co nitrides ($Ni_xCo_{3-x}N$) solid-solutions decorated on nitrogen doped carbon nanotubes (NCNT) were designed and synthesized the first time as highly stable bi-functional ORR and OER electrocatalysts for Zn-air batteries. The NCNTs provided a conductive and porous framework for fast ion and electron diffusion to enhance mass-transport. Additionally, they provided a physical support that helped stabilize the $Ni_xCo_{3-x}N$ nanostructures. Computational simulations showed that a wide range of compositions could be achieved by simply changing the Ni/Co contents, as the Ni and Co cations share similar kinetic diameters, are mutually soluble (without the formation of any intermetallic phase) and the formation energy of the bimetal alloy nitrides are also on a similar level. Guided by the theoretical calculations, the optimised Ni/Co ratio nitride (*i.e.*, $Ni_{0.5}Co_{2.5}N$, the corresponding hybrid sample with NCNT is subsequently denoted as SS/NCNT) possesses balanced and improved ORR/OER bi-functional properties. Analogous experimental and theoretical activity trends in the ORR and OER performances were observed for a series of $Ni_xCo_{3-x}N$ solid-solutions (x=0, 0.5, 1, 1.5, 2, 2.5 and 3). Compared with other Ni/Co nitrides, the results show that $Ni_{0.5}Co_{2.5}N$ possessed the weakest transition metal-nitrogen (TM-N) bonds as the bonding states are shifted closer to the Fermi level in the bulk structure and N atoms on the surface are in more charge rich states compared with other composites. For these reasons, the activation energy among catalysts (both transition metal and N atoms) and reactants/intermediates could be optimized by changing the ratio of Ni and Co in the solid solution nitrides. Both the unique composition and structural design delivered one of the highest performing ORR/OER catalytic properties ever reported, showing better catalytic performances to commercial noble metals, and with much enhanced stability, as they presented no obvious current density decay after extended cycling. To demonstrate practical efficacy, a rechargeable Zn-air battery using SS/NCNT as the air-cathode materials exhibited a steady current density of ~5 mA cm^{-2} for more than 300 cycles.

The synthetic procedure to make solid-solution nitrides decorated with NCNT includes the following three steps, as shown in Scheme 1 and detailed in the Supplementary information (SI). Firstly, the commercial multi-walled carbon nanotubes were mildly oxidized (oxCNT) to increase the number of oxygen functional groups by an improved Hummers' method [28]. Oxygen functional species can form a strong interaction with metal cations for nucleation and further growth of nanostructures. Then, $Ni(NO_3)_2.6H_2O$ and $Co(NO_3)_2.6H_2O$ with different Ni:Co mole ratios (3:0; 2.5:0.5; 2:1; 1.5:1.5; 1:2; 0.5:2.5 and 0:3) were hydrolysed on the surface of the pre-treated carbon nanotubes. The complex reaction involving Ni/Co and nitrogen functional groups from methenamine was subsequently conducted in a mixed alcoholic solution at 80 °C. After that, the hydrothermal reaction results in the formation of Ni/Co hydroxide nanostructures on the oxCNT. Finally, the $Ni_xCo_{3-x}N$/NCNT was formed by annealing the hydroxides/oxCNT under a flow of ammonia gas at a specific temperature range. The composition of the $Ni_xCo_{3-x}N$ could be tuned on an atomistic level, given the high solubility and interchangeable nature of Co and Ni within the lattice, in order to optimize the bi-functional properties of the electrocatalysts.

The nanostructures of the as-synthesized materials were imaged by scanning electron microscopy (SEM) and transmission electron microscopy (TEM). The TEM images in Fig. S1a shows that, after hydrothermal reactions, Ni/Co hydroxides nanosheets typically grew on the oxCNT, forming an interwoven network. As the annealing temperature was increased under a flow of ammonia gas, the morphologies of the uniform nanosheets tended to change to nanoparticles attached to the NCNT support (Fig. S1 b–f). Meanwhile, thermogravimetric analysis of the products after the hydrothermal reaction (Fig. S2) confirmed the release of gas and significant weight loss at around 300 °C. From 500 °C and above, nanoparticles size (ranging from ~20–50 nm), morphology and crystallinity did not vary substantially (Fig. S3); where all materials adopted a hexagonal Ni_3N structure ($P6_322$). As no substantial difference in structure or catalytic activity was observed in materials annealed at temperatures above 500 °C, a series of solid-solutions were grown at a fixed annealing temperature of 500 °C, which overall, constitutes a relatively economic synthetic route to the formation of $Ni_xCo_{3-x}N$/NCNT. BET surface areas of representative samples before

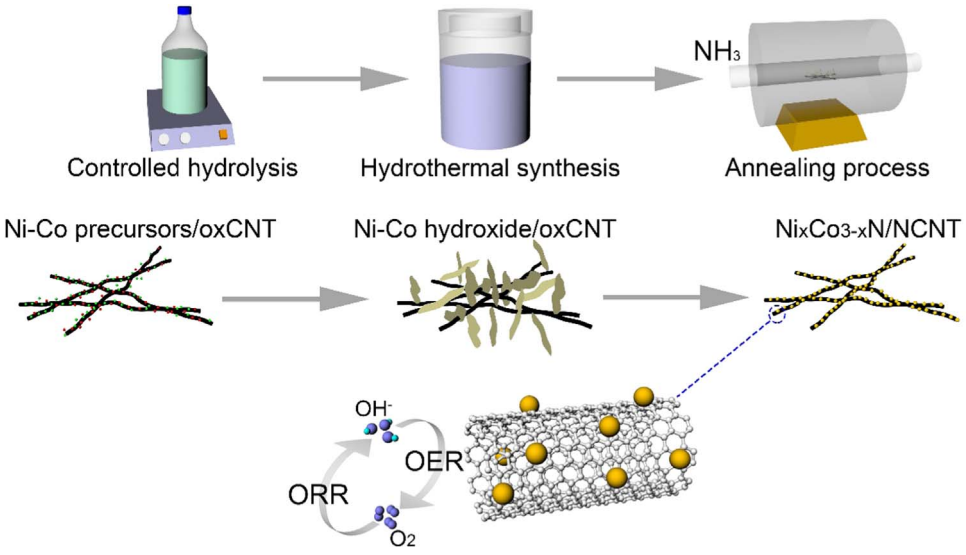

Scheme 1. Synthetic process of the NCNT supported $Ni_xCo_{3-x}N$ solid solution.

and after the ammonia annealing process were examined and compared (Fig. S4). The results showed that typical $Ni_xCo_{3-x}N$/NCNT exhibited specific surface area of ~90 m^2 g^{-1}, slightly lower than that of hydroxide counterparts (~110 m^2 g^{-1}). It is worth noting that the degas temperature of the BET tests was set at 80 °C to avoid a morphology change in the as-made hydroxide materials. As such, the calculated specific surface areas were systematically underestimated. As for the electrochemically active surface area (ECSA) calculated from double-layer capacitance measurements (Fig. S5), typically $Ni_xCo_{3-x}N$/NCNT possesses almost double the ECSA of Ni/Co hydroxides/oxCNT, indicating that the ammonium-treatment process increased the ECSA of the hybrids. The micromorphology of the typical $Ni_xCo_{3-x}N$/NCNT was further examined by SEM as shown in Fig. 1a and b. The grass-like structure with multi-scaled porosity can likely facilitate fast gas/ion diffusion, further proved by low magnification TEM image in Fig. S6. The distribution of the elements in the hybrid materials was interrogated by energy dispersive spectroscopy (EDS) using a scanning TEM (STEM) (Fig. 1c–g). The main elements, Co and Ni, were well dispersed across the surface of the CNT support and overlapped strongly. X-ray diffraction (XRD) patterns of a series of the samples shown in Figures S7a and Fig. 1h showed that the series of $Ni_xCo_{3-x}N$ (x=0, 0.5, 1, 1.5, 2, 2.5, and 3) adopted a hexagonal Ni_3N structure ($P6_322$). According to the Scherrer equation, these nanostructures have similar crystal sizes, ranging between 30–50 nm, analogous to the particle sizes observed by TEM. With an increase in Ni content peaks shifted to higher angles, associated with a decrease in unit cell volume consistent with Vegard's law (Fig. S7b). These results provided strong evidence for the formation of nanoparticulate solid-solutions of Co-Ni nitrides. Further, the Ni/Co atomic ratio (Table S1) of these materials were detected by SEM-EDS for the bulk structure, and showed a matching value of the raw ratio used in the synthesis.

The geometries of the $Ni_xCo_{3-x}N$ composition were studied using Density Functional Theory (DFT) calculations, for x=0, 0.5, 1, 1.5, 2, 2.5, and 3. Detailed computational settings are described in the SI. The experimental lattice parameters for the bi-metal nitrides are lacking in the literature, so the pure Ni_3N, which has been comprehensively studied experimentally, was selected as the reference to evaluate our computational settings. As listed in Table S2, the optimized lattice parameters were in line with previous theoretical predictions [29–31]. Compared with the experimental data [30], the mismatch was below 0.23%. Further, a 2 × 2 × 2 supercell of Ni_3N was adopted to study its magnetic properties, as nickel behaves ferromagnetically. Our calculations reveal that the nickel nitride is non-magnetic, which is in line with previous experimental observations [32,33]. From Bader analysis [34,35], the valence charge of the Ni atom is 9.64. Collectively, these results provided confidence to carry out the $Ni_xCo_{3-x}N$ calculations by substituting Ni with Co in the ε-Fe_3N structure ($P6_322$). The configurations of the lowest energy for $Ni_xCo_{3-x}N$ are shown in Figures S8 and S9. The Ni and Co atoms are keen to occupy the opposite position within the same octahedral N central, which corresponds to mixed areas of Ni and Co from EDS mapping images observed experimentally. The formation energies of the bi-metal nitrides were calculated based

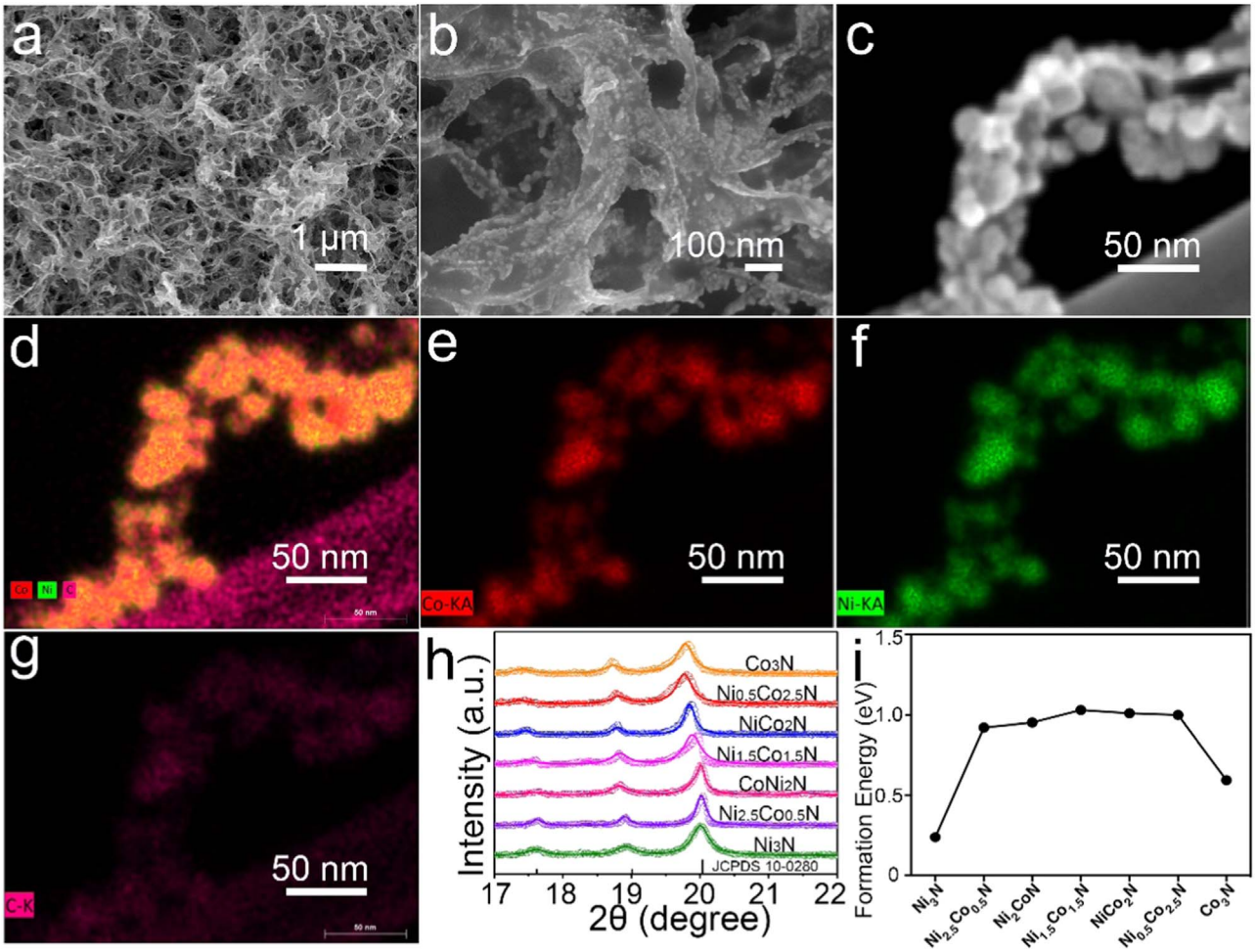

Fig. 1. Low (a) and high (b) magnification SEM images of typical $Ni_xCo_{3-x}N$/NCNT composites; (c-g) elemental mapping images in a typical $Ni_xCo_{3-x}N$/NCNT hybrid, (c) STEM image recorded by the high angle annular dark field (HAADF) detector. EDS maps of (d) mixed elements, (e) Co, (f) Ni and (g) C in a typical $Ni_xCo_{3-x}N$/NCNT; (h) Experimentally observed XRD patterns and corresponding standard pattern (JCDPS No. 10–0280) and (i) theoretical calculations of the formation energy for the series of $Ni_xCo_{3-x}N$/NCNT solid-solutions studied herein (x=0, 0.5, 1, 1.5, 2, 2.5, and 3).

on the following equation:

$$E_f = E_{Ni_xCo_{3-x}N} - xE_{Ni} - (3-x)E_{Co} - E_N \quad (1)$$

where $E_{Ni_xCo_{3-x}N}$ is the energy of the nitrides, and E_{Ni}, E_{Co} and E_N are the chemical energies for Ni, Co and N, respectively. As shown in Fig. 1i, the pure Ni_3N compound possesses the lowest formation energy, followed by pure Co_3N. For all bi-metal interstitial nitrides, the energy penalty is substantially higher than the pure materials but range very little over the bi-metallic region from 0.92 to 1.03 eV per unit cell. This indicates that these bi-metal nitrides could be formed with any Ni/Co ratio. The Density of States (DOS) of the series of $Ni_xCo_{3-x}N$ in bulk structures reveal that all nitrides are metallic, shown in Fig. S10 (a-g). Moreover, the 2p orbital of N hybridized with 3d orbitals Ni and Co in the conduction band and the valenced band contributed mainly by transition metals. Compared to Ni, more notable contribution from Co is observed to influence the peak position and width in the valence band. As in $Ni_{0.5}Co_{2.5}N$, it possessed the weakest TM-N bonds due to the fact that the bonding states are shifted closer to the Fermi level compared with other composites. This result is consistent with the Bader Charge Analysis, shown in Fig. S10h. The bulk structural evolution could highly affect catalytic properties, which provide the prerequisite to tune the bifunctionality of different compositions of Co and Ni.

Taking the $Ni_{0.5}Co_{2.5}N$ as a model, its charge distribution at the Fermi level (Fig. 2a) showed the metallic bonding behaviour. The chemical compositions and valence states of SS/NCNT can be confirmed experimentally using X-ray photoelectron spectroscopy (XPS) in Fig. 2b-f. As illustrated in Fig. 2b, the C 1 s peak shows carbon-nitrogen (and oxygen) bonds at ~285.6 eV, indicating successful nitrogen doping of defect-rich carbon nanotubes [36]. It is widely known that nitrogen-doped carbon materials can be beneficial for oxygen electrocatalysis [16]. In addition, the N 1 s region (Fig. 2c) shows peaks at 400 and 402.9 eV that correspond to absorbed N_2, interstitial nitrogen dopants and oxidised surface nitrogen respectively on NCNT [16,37,38]. The strong peak at ~398.1 eV corresponds to the metallic Ni/Co and nitrogen bonds [14]. The Ni 2p region (Fig. 2d) shows a multiplet-split Ni 2p3/2 peak (centered at ~873.4 and ~870.3 eV), a multiplet-split Ni 2p1/2 peak (~855.6 and ~852.5 eV) and a pair of satellite peaks (ΔNi=17.8 eV), which corresponds to the mixed valence states of +2 and +1 Ni at the material surface [39]. Fig. 2e shows the Co 2p region. Similar to Ni 2p region, the Co 2p peaks also contains spin-orbit doublets (ΔCo=15.0 eV). The doublets consist of two pairs of peaks and one pair of satellite peak in lower (Co 2p3/2) and higher (Co 2p1/2) energy bands centred at 803.0 and 785.9 eV, respectively, suggesting the same varied valence states as Ni. The atomic ratio of metal to nitrogen on the material surface, as measured by XPS, was 2.6: 1. This was substantially lower than the metal to oxygen ratio (~11: 1), suggesting negligible oxidation of the metal nitride surface under ambient conditions. The Ni/Co ratios on the surface of these solid solution nitrides were measured through XPS, and the results showed a similar trend to that seen in the bulk structure (Table S1). To identify the catalytic sites of these $Ni_xCo_{3-x}N$ surfaces, the HRTEM images (Fig. S11) suggested that the (111) plane was the dominant exposed lattice plane in both Co_3N and Ni_3N. For theoretical calculations, models were built on using a (111) surface with six layers of atoms with the bottom half was fixed while all others were fully relaxed. The projected density of states (pDOS) of surface atoms of each solid solution nitride were calculated to determine the reactive sites, shown in Fig. 2f and Fig. S12. The surface atom denotations are shown in Fig. S13 to distinguish each contribution. Both N_top and N_surface atoms could act as highly reactive sites. Transition metal-surface atoms have the highest density at the Fermi level, and thus they were selected as the reactive sites for the calculations of binding of all of the intermediates.

The electrocatalytic performance was investigated by linear sweep voltammetry (LSV) using a rotating disk electrode (RDE) in oxygen-saturated KOH electrolyte. Linear sweep voltammograms (LSV) measurements of SS/NCNT were conducted at different RDE rotation rates (Fig. 3a). The kinetic process was analysed by using the Koutecky-Levich (K-L) equation for SS/NCNT (Fig. S14), the calculated electron transfer number (n) is ~4 at a potential of 0.5 V *vs.* RHE, which is better than that of Pt/C (~3.92) and other $Ni_xCo_{3-x}N$/NCNT materials (Figs. S15, S16), indicating a complete four-electron transfer pathway.

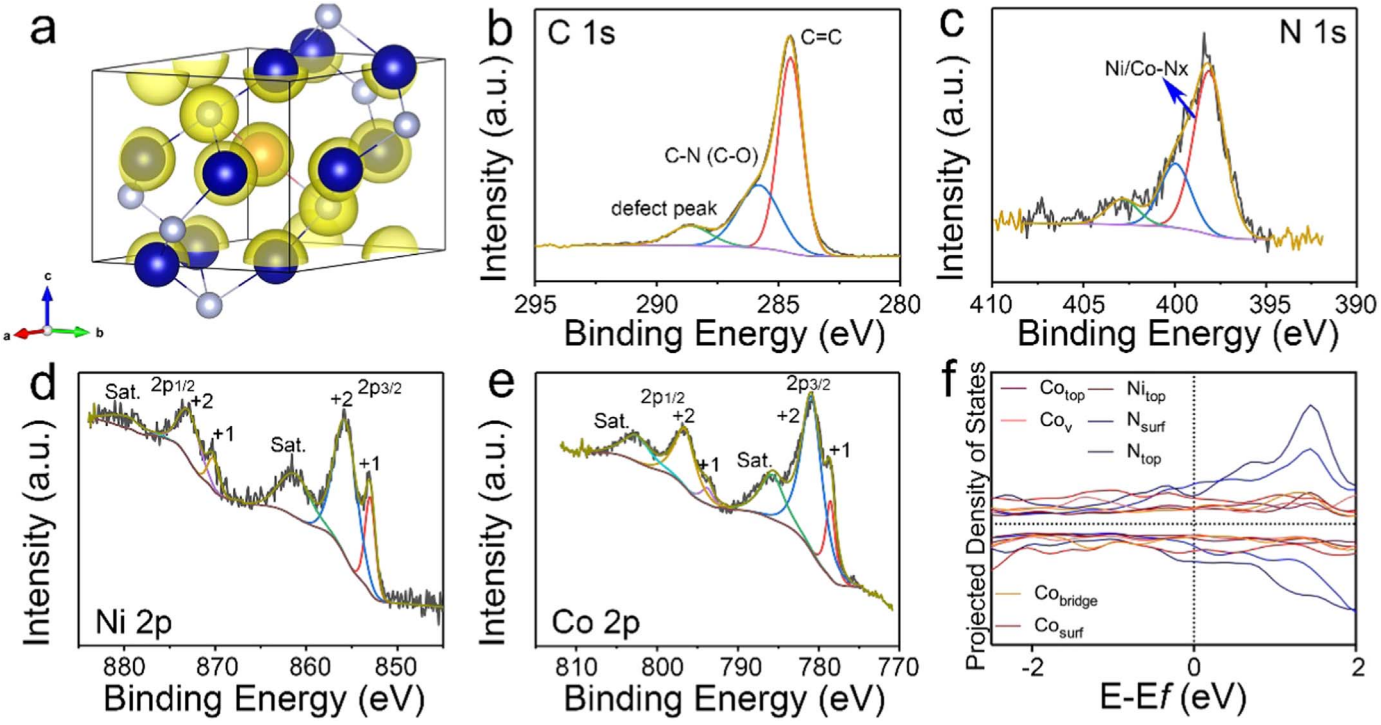

Fig. 2. (a) The charge distribution of the Fermi level of $Ni_{0.5}Co_{2.5}N$. The isosurface is set to 0.2 e/r_0^3, where r_0 is the Bohr radii. The salmon, blue and grey balls represent Ni, Co, and N atoms, respectively; XPS spectrum for SS/NCNT sample of (b) C 1s; (c) N 1 s; (d) Ni 2p and (e) Co 2p, respectively. (f) The projected density of states of the surface atoms of $Ni_{0.5}Co_{2.5}N$ (111) surface.

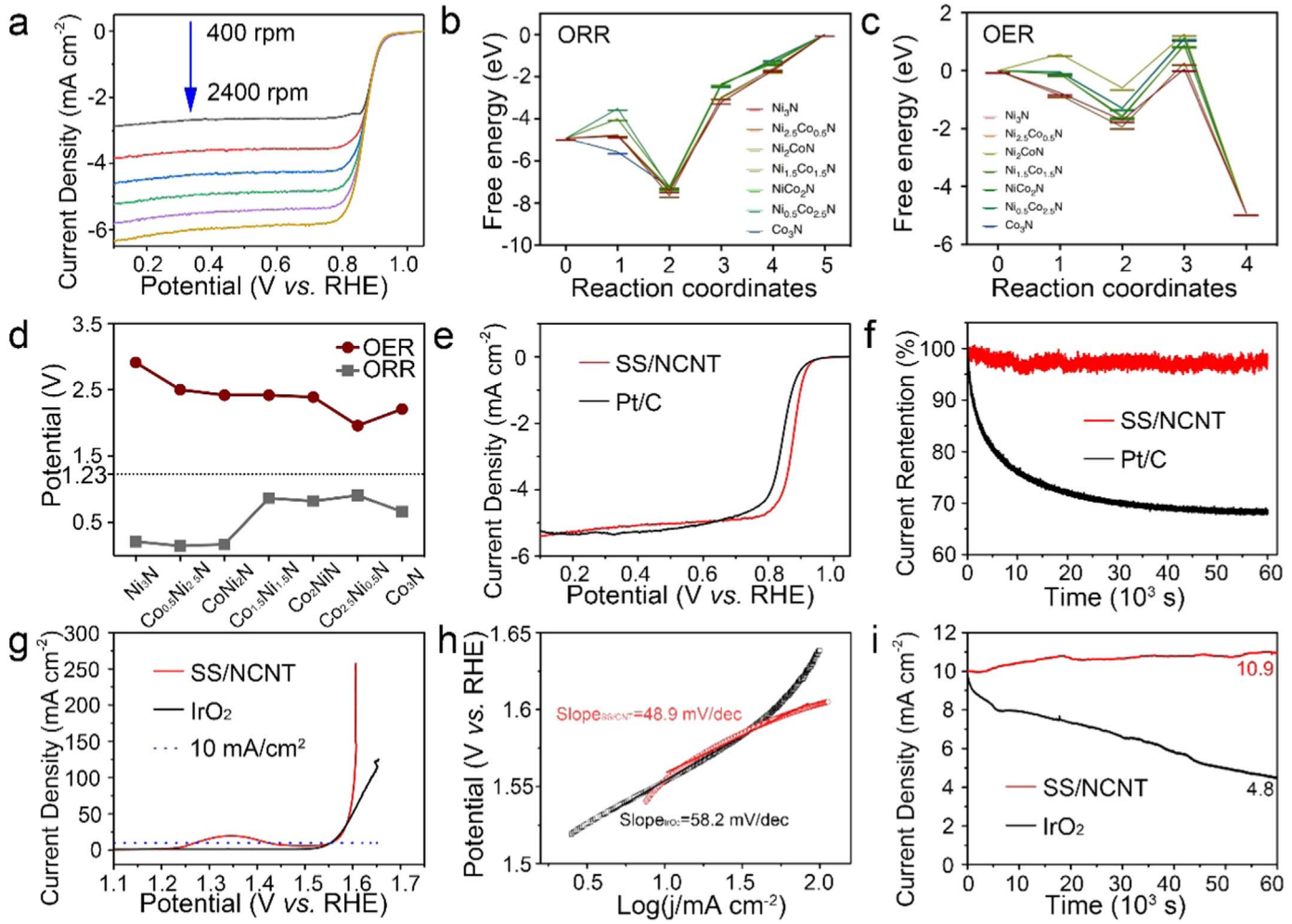

Fig. 3. (a) Linear sweep voltammograms (LSV) tests of SS/NCNT in 0.1 M KOH at different rotation rates (400–2400 rpm); free energy of ORR (b) and OER (c) in elementary steps for the series of $Ni_xCo_{3-x}N$ on the (111) surface. (d) the potential required for ORR/OER reaction for the series of $Ni_xCo_{3-x}N$. (e) comparison of the SS/NCNT and commercial Pt/C for ORR performances in 0.1 M KOH by using LSV test at a rotation speed of 1600 rpm; (f) stability test for the ORR of SS/NCNT and commercial Pt/C, respectively; (g) LSV curves for OER; (h) Tafel plots transferred from LSV curves; (i) stability test for the OER of SS/NCNT and commercial Pt/C, respectively.

Hence, DFT calculations were carried out based on a four-electron pathway mechanism for both ORR and OER, proposed as follows and further demonstrated by *in-situ* Raman studies (Fig. S17):

For ORR, the complete reaction can be summarized in the following steps:

$$O_2 + * \rightarrow O_2^* \quad (2)$$

$$O_2^* + H_2O(l) + e^- \rightarrow OOH^* + OH^- \quad (3)$$

$$OOH^* + e^- \rightarrow O^* + OH^- \quad (4)$$

$$O^* + H_2O(l) + e^- \rightarrow OH^* + OH^- \quad (5)$$

$$OH^* + e^- \rightarrow * + OH^- \quad (6)$$

In an alkaline environment, OER could occur by the following pathways:

$$OH^- + * \rightarrow OH^* + e^- \quad (7)$$

$$OH^* + OH^- \rightarrow O^* + H_2O(l) + e^- \quad (8)$$

$$O^* + OH^- \rightarrow OOH^* + e^- \quad (9)$$

$$OOH^* + OH^- \rightarrow * + O_2(g) + H_2O(l) + e^- \quad (10)$$

where * stands for an active site, (l) and (g) refer to liquid and gas phases, respectively. O*, OH*, and OOH* are the binding intermediates.

For each reactive step for overall $Ni_xCo_{3-x}N$, the adsorption of O_2 for ORR is the rate determining step, and the formation of OOH* is the limiting step for OER (Fig. 3b and c). The ORR catalytic reactions for this series of $Ni_xCo_{3-x}N$/NCNT hybrids were compared and are shown in Fig. S18; they show the same trend as for theoretical predictions (Fig. 3d). $Ni_{0.5}Co_{2.5}N$ possesses the narrowest potential between ORR and OER and was the best performer as a bifunctional catalyst. Further analysis from the surface of the catalysts indicated that besides the modified bonds of TM-N in the bulk analysis, the valence charge of the surface atoms also varies and does not linearly change with the ratio (Fig. S19). Overall, the nitrogen at the surface position (N_surf) possessed more electrons than the top position (N_top). This might be because the N_surf atoms are bonded with four transition metal atoms, whereas the N_top atoms are octahedrally bonded with three transition metal atoms. It also indicated that those transition metals bonded with the N_surf atoms were in higher charge-deficient states. Among all the $Ni_xCo_{3-x}N$ series, the $Ni_{0.5}Co_{2.5}N$ composition is the one in which transition metal atoms are in a more charge-deficient state. From both surface and bulk structure analysis, the synergistic effect during catalytic processes can be attributed to both bulk-surface response and separated surface charge engineering realized by controlled Ni/Co atomic ratios in the nitrides. Hence, the $Ni_{0.5}Co_{2.5}N$ composition delivered the weakest TM-N bonds in bulk and the highest charge-deficient states of transition metal atoms at the surface, which helps facilitate the most desirable catalytic property [40–42]. The best

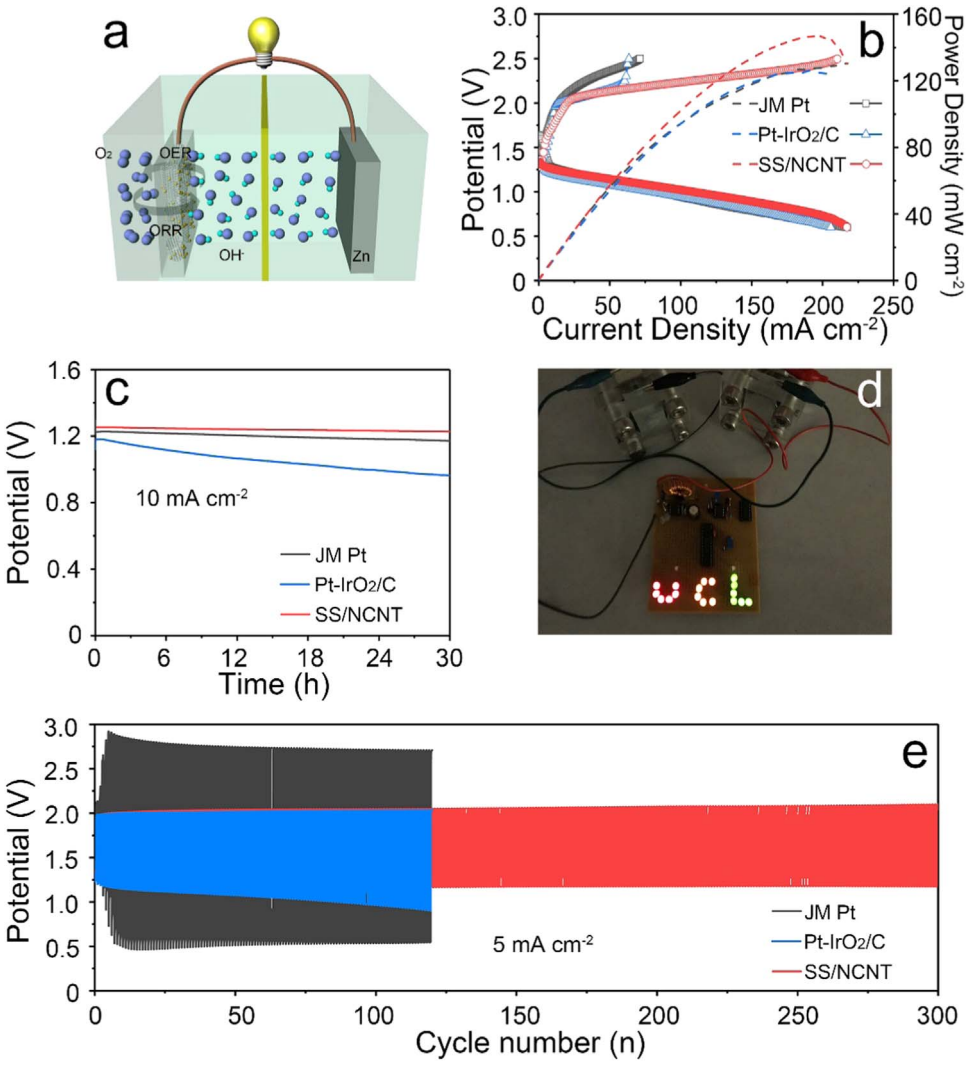

Fig. 4. (a) Schematic illustration of a Zn-air battery; (b) polarization curves of the as-fabricated Zn-air battery by using Pt on carbon paper made from Johnson Matthey (JM Pt), commercial Pt-IrO_2/carbon on carbon paper (Pt-IrO_2/C) and SS/NCNT on carbon paper as air-cathodes, respectively; (c) galvanostatic discharge curves of the Zn-air batteries using different catalysts as air-cathodes, respectively; (d) digital camera picture of the two Zn-air batteries in series powering the LED lights; (e) cycling performance of the Zn-air batteries at 5 mA cm^{-2}.

ORR performing sample SS/NCNT with a Ni/Co ratio of 0.5/2.5, was then compared with a commercial Pt/C catalyst, as shown in Fig. 3e. The half-wave potential for SS/NCNT is ~30 mV more positive than that of Pt/C. Moreover, those two catalysts exhibited similar limiting current density, suggesting SS/NCNT is an excellent ORR electrocatalyst with faster kinetics and comparable diffusivity compared with Pt/C. The current-time chronoamperometric responses (CA) were investigated for SS/NCNT and Pt/C at −0.45 V in O_2-saturated 0.1 M KOH shown in Fig. 3f to assess durability. After 60,000 s, more than 98% of the initial current density is retained for the SS/NCNT catalysts, much higher than that of Pt/C (less than 70% retention of original current density), suggesting its excellent stability as an ORR catalyst. Meanwhile, the OER activities were also evaluated among different compositions of solid solutions, showing the similar trend as theoretical predictions (Fig. S20). The best performer SS/NCNT was compared to a commercial IrO_2 catalyst. Higher concentrated electrolyte (1 M KOH) was chosen to increase the mass transport during the reaction thus enlarging the discrepancy of catalytic performance. As shown in Fig. 3g, the potential to reach the current density of 10 mA/cm^2 can be estimated as 1.554 V for SS/NCNT, almost the same value as that of IrO_2 (1.553 V). Remarkably, the current density increased dramatically with an increase of overpotential for SS/NCNT. The smaller Tafel slope of SS/NCNT further demonstrated its superior kinetic OER catalytic performance (Fig. 3h). The stability investigation of OER catalytic performances was implemented by chronoamperometric response at ~1.55 V *vs*. RHE in Fig. 3i, at which potential, both catalysts can reach the initial current density of ~10 mA cm^{-2}. After 60,000 s, the current density of SS/NCNT increased to 109% of the initial value, more than twice that of IrO_2 (48% retention). These results indicated that the increased performance of SS/NCNT for OER works over long-term conditions. The presented excellent bi-functional electrocatalytic properties made the SS/NCNT one of the top-tier catalysts amongst these reported as state-of-the-art (Tables S3 and S4). To uncover the mechanisms beyond performance evolutions of SS/NCNT after long-term working tests, electrodes with an area of ~1 cm^2 were prepared using the same areal loading of SS/NCNT on hydrophobic carbon papers with gas diffusion layers. The morphologies, phases and chemical compositions were analyzed following the CA tests for both ORR and OER reactions. SEM images in Fig. S21 show that the interwoven NCNTs with dense nanoparticles have no obvious morphological change after both ORR and OER reactions. Furthermore, the new peak at ~291.6 eV in both C 1 s spectra corresponded to organics containing C-F groups from the Nafion membranes (Figs. S22a, S23a) [43]. In addition, in both Co 2p and Ni 2p spectra, surface oxidation states increase from a mixture of +1 and +2 to mixed +2 and +3 states (Figs. S22b, S22c, S23b, S23c), which implies that higher oxidation

states of Ni or Co are more favorable for the higher electrocatalytic activity observed herein, especially during the OER process [44,45]. Compared to the pristine N 1 s spectrum and the one after ORR stability testing (Figs. S22d), new peaks are observed (Fig. S23d) at ~403 and ~406.5 eV, which can be assigned to higher oxidation state surface N groups. During the oxygen electrocatalytic process, the surface of the catalysts is oxidized, forming Ni/Co hydroxides species, $-NO_2$ and/or $-NO_3$ groups [46]. However, the main peaks of Ni/Co nitrides are retained in the XRD patterns (Fig. S24) alongside the Ni/Co-N bonds in N 1s XPS, which further illustrated the stability of the $Ni_xCo_{3-x}N$ in the structures. Moreover, the hydroxides with higher valence states of Ni/Co species, provide more active catalytic surfaces for the OER (where the Ni/Co nitride bulk framework likely improves electron conductivity due to its metallic nature), thus improving catalytic performance. To represent a more realistic environment, where the surface would form a thin layer of oxide/hydroxide during the electrochemical oxidation of water [47,48]. The $Ni_{0.5}Co_{2.5}N$ (111) was further modelled to saturate with -O and -OH, and are shown in Fig. S25a. After the surface oxidation, the changes of valence charge of the surface atoms are obvious (Fig. S25b). The valence charge of Co_top and Co_surf atoms remain unchanged, while other Co positions and nitrogen are significantly reduced. It suggests that the oxidation could increase the charge-deficient states of transition metal atoms while weakening the TM-N bonds at the same time, which further boost the performance in OER.

To assess the actual application of SS/NCNT as bi-functional oxygen electrocatalysts, rechargeable Zn-air batteries were assembled. As shown by schematic illustration in Fig. 4a, a piece of Zn foil was used as the anode and the catalysts-loaded superhydrophobic carbon paper with a gas diffusion layer were prepared as the air-cathodes. To compare with the commercial Pt-coated carbon paper from Johnson Matthey (Product No. ELE00162; loading density: 0.4 mg cm^{-2}), the mass density of the catalysts was controlled to be the same for SS/NCNT and commercial Pt-IrO_2/C. 6 M KOH containing 0.2 M of $Zn(CH_3COO)_2$ was chosen as the electrolyte to guarantee the reversible redox reaction between Zn and Zn^{2+}, further proved by Fig. S26. The open circuit potentials (Fig. S27) for Zn-air batteries by using Pt on carbon paper made from Johnson Matthey (JM Pt), commercial Pt-IrO_2/carbon loaded carbon paper (Pt-IrO_2/C) and carbon paper supported as-synthesized catalysts (SS/NCNT) as air-cathodes are within the range of 1.35–1.4 V, suggesting similar values for these commercial Zn-air batteries and provides validity for the as-fabricated batteries. Polarization plots of the batteries in Fig. 4b presented the relatively higher discharge current densities and the lower charge/discharge voltage gap of SS/NCNT compared to commercial noble metal catalysts and electrodes. Moreover, the maximum power density of the Zn-air battery using SS/NCNT catalysts were as high as 147 mW cm^{-2}, exceeding commercially available noble metal catalysts/electrodes (130 mW cm^{-2} for JM Pt and 125 mW cm^{-2} for Pt-IrO_2/C). The galvanostatic discharge curves at a current density of 10 mA cm^{-2} (Fig. 4c) showed higher discharge potential of 1.245 V for the Zn-air battery with SS/NCNT catalysts, and retention at 1.228 V after 30 h, superior to that of the counterparts. The calculated energy density and specific capacity during discharge process are 931.7 Wh/Kg and 758.5 mAh g^{-1} for Zn-air battery with SS/NCNT on air-cathodes from Fig. S28. Several Zn-air batteries with SS/NCNT catalysts were assembled with the purpose to satisfy specific energy supply for actual applications. As presented in Fig. 4d, two Zn-air batteries based on SS/NCNT connected in series can be used to power a circuit containing the UCL logo in LED lights. To further evaluate the rechargeability of the Zn-air batteries based on different air-cathodes, cyclic galvanostatic discharge-charge measurements were performed at a current density of 5 mA cm^{-2} in Fig. 4e. The Zn-air battery with SS/NCNT air-cathodes exhibited an initial discharge potential of 1.30 V and charge potential of 1.91 V (enlarged area in Fig. S29), with much smaller charge/discharge voltage gap of 0.61 V and higher round-trip efficiency of ~68.1% compared to commercial products. Even after 300 cycles (50 h) without replacing the Zn anode or the electrolyte, the Zn-air battery with SS/NCNT catalyst showed only a slight performance decay with an increase in the charge/discharge voltage gap of 0.3 V; whereas Pt-IrO_2/C catalysts and Pt JM electrodes exhibited an increase of 0.4 V and 1.32 V, respectively, after 120 cycles under the same conditions. SEM (Fig. S30) and XPS (Fig. S31) results of the air-cathodes after cycling performance indicated the similar compositional evolution and structural integrity compared to single ORR and OER processes. Furthermore, Zn-air batteries in this work exhibited comparable performance compared to other reported work. (Table S5). These results demonstrate that the as-designed SS/NCNT catalysts can be promising alternatives to commercial noble metal materials for bi-functional ORR and OER electrocatalysts.

In summary, a series of $Ni_xCo_{3-x}N$/NCNTs hybrids have been developed as low-cost high-performance substitutes for commercial noble metal-based oxygen electrocatalysts. By coupled theoretical and experimental approaches, the compositions of the Ni and Co solid solution nitrides were analysed, optimised and controlled from the atomistic level. The multiple active sites and critical limiting steps were identified during catalytic processes. Then, specific ORR and OER activities were tailored by optimization of the ratio of Ni/Co in nitrides *via* bulk-surface response and separated surface charge distribution. Detailed structural analysis of the catalysts, both before and after ORR and OER reactions revealed that the Ni/Co hydroxides partially form, which are more active catalytic species for the OER. Moreover, the residual $Ni_xCo_{3-x}N$ provided a conduit for metallic electron conductivity that enhanced the catalytic performance. DFT simulation indicated that surface oxidation could increase the charge-deficient states of transition metal atoms while weaken the TM-N bonds at the same time. By utilizing the as-designed SS/NCNT catalysts in a rechargeable Zn-air battery configuration, the air-cathode outperformed commercial noble metal catalysts and electrodes in both rechargeability and durability. In addition, this work should stimulate further research on multiple-component nitrides for electrocatalysts in energy storage and conversion devices, and for *in-situ* studies of their catalytic mechanism. Theoretical work will focus on the kinetic interactions between surface modified layers with transition metal nitrides and alternative intermediates and pathways during each reaction.

Author contributions

G. He and X. Han contributed equally. G. He designed the projects and carried out the experiments. X. Han carried out simulations; B. Moss and Z. Weng performed the morphology tests; S. Gadipelli contributed to the TGA measurements and analysis; G. He and F. Lai performed the battery fabrication; A. Kafizas performed the analysis of XRD results; I. P. Parkin, H. Wang, Z. X. Guo and D. Brett supervised the project. G. He, X. Han and I. P. Parkin co-wrote the manuscript. All authors discussed the results and contributed to manuscript revision.

Acknowledgements

Prof. G. Sankar, Dr. N. Mansor and Mr. R. Lin are acknowledged for their useful suggestion in crystal structure, electrochemistry and figure presentation. The authors would like to thank the Science and Technology Facilities Council, UK (ST/N002385/1) for STFC/MDC Futures Early Career Award; Engineering and Physical Sciences Research Council, UK (EP/L015862/1, EP/N032888/1, EP/K002252/1, EP/L018330/1 and EP/K021192/1) for the financial support. The authors acknowledge the use of the UCL Grace High-Performance Computing Facility (Grace@UCL), and associated support services, in the completion of this work.

Conflicts of interests

The authors declared no conflicts of interests.

Appendix A. Supporting information

Supplementary data associated with this article can be found in the online version at doi:10.1016/j.ensm.2018.08.020.

References

[1] P.D. Luna, J. Wei, Y. Bengio, A. Aspuru-Guzik, E.H. Sargent, Use machine learning to find energy materials, Nature 552 (2017) 23–25.
[2] A. Bernstein, E.H. Sargent, A. Aspuru-Guzik, R. Cogdell, G.R. Fleming, R.V. Grondelle, M. Molina, Renewables need a grand-challenge strategy, Nature 538 (2016) 30.
[3] N.T. Suen, S.F. Hung, Q. Quan, N. Zhang, Y.J. Xu, H.M. Chen, Electrocatalysis for the oxygen evolution reaction: recent development and future perspectives, Chem. Soc. Rev. 46 (2017) 337–365.
[4] Y. Li, M. Gong, Y. Liang, J. Feng, J.E. Kim, H. Wang, G. Hong, B. Zhang, H. Dai, Advanced zinc-air batteries based on high-performance hybrid electrocatalysts, Nat. Commun. 4 (2013) 1805.
[5] Y. Yang, K. Zhang, H. Lin, X. Li, H.C. Chan, L. Yang, Q. Gao, MoS_2–Ni_3S_2 heteronanorods as efficient and stable bifunctional electrocatalysts for overall water splitting, ACS Catal. 7 (2017) 2357–2366.
[6] Y.P. Zhu, T.Y. Ma, M. Jaroniec, S.Z. Qiao, Self-templating synthesis of hollow Co_3O_4 microtube arrays for highly efficient water electrolysis, Angew. Chem. Int. Ed. Engl. 56 (2017) 1324–1328.
[7] L. Bu, N. Zhang, S. Guo, X. Zhang, J. Li, J. Yao, T. Wu, G. Lu, J.-Y. Ma, D. Su, X. Huang, Biaxially strained PtPb/Pt core/shell nanoplate boosts oxygen reduction catalysis, Science 354 (2016) 1410–1414.
[8] S. Kumari, B.P. Ajayi, B. Kumar, J.B. Jasinski, M.K. Sunkara, J.M. Spurgeon, A low-noble-metal $W_{1-x}Ir_xO_{3-\delta}$ water oxidation electrocatalyst for acidic media via rapid plasma synthesis, Energy Environ. Sci. 10 (2017) 2432–2440.
[9] G.A. Ferrero, K. Preuss, A. Marinovic, A.B. Jorge, N. Mansor, D.J. Brett, A.B. Fuertes, M. Sevilla, M.-M. Titirici, Fe-N-doped carbon capsules with outstanding electrochemical performance and stability for the oxygen reduction reaction in both acid and alkaline conditions, ACS Nano 10 (2016) 5922–5932.
[10] F. Meng, H. Zhong, D. Bao, J. Yan, X. Zhang, In situ coupling of strung Co_4N and intertwined N-C fibers toward free-standing bifunctional cathode for robust, efficient, and flexible Zn-air batteries, J. Am. Chem. Soc. 138 (2016) 10226–10232.
[11] F. Cheng, J. Shen, B. Peng, Y. Pan, Z. Tao, J. Chen, Rapid room-temperature synthesis of nanocrystalline spinels as oxygen reduction and evolution electrocatalysts, Nat. Chem. 3 (2011) 79–84.
[12] B.Y. Xia, Y. Yan, N. Li, H.B. Wu, X.W. Lou, X. Wang, A metal–organic framework-derived bifunctional oxygen electrocatalyst, Nat. Energy 1 (2016) 15006.
[13] C. Tang, B. Wang, H.F. Wang, Q. Zhang, Defect engineering toward atomic Co-N_x-C in hierarchical graphene for rechargeable flexible solid Zn-air batteries, Adv. Mater. 29 (2017) 1703185.
[14] S. Dou, L. Tao, J. Huo, S. Wang, L. Dai, Etched and doped Co_9S_8/graphene hybrid for oxygen electrocatalysis, Energy Environ. Sci. 9 (2016) 1320–1326.
[15] P. Chen, T. Zhou, L. Xing, K. Xu, Y. Tong, H. Xie, L. Zhang, W. Yan, W. Chu, C. Wu, Y. Xie, Atomically dispersed iron-nitrogen species as electrocatalysts for bifunctional oxygen evolution and reduction reactions, Angew. Chem. Int. Ed. Engl. 56 (2017) 610–614.
[16] G.-L. Chai, K. Qiu, M. Qiao, M.-M. Titirici, C. Shang, Z.X. Guo, Active sites engineering leads to exceptional ORR and OER bifunctionality in P, N Co-doped graphene frameworks, Energy Environ. Sci. 10 (2017) 1186–1195.
[17] A. Aijaz, J. Masa, C. Rosler, W. Xia, P. Weide, A.J. Botz, R.A. Fischer, W. Schuhmann, M. Muhler, Co@Co_3O_4 encapsulated in carbon nanotube-grafted nitrogen-doped carbon polyhedra as an advanced bifunctional oxygen electrode, Angew. Chem. Int. Ed. Engl. 55 (2016) 4087–4091.
[18] Y. Zhang, X. Fan, J. Jian, D. Yu, Z. Zhang, L. Dai, A general polymer-assisted strategy enables unexpected efficient metal-free oxygen-evolution catalysis on pure carbon nanotubes, Energy Environ. Sci. 10 (2017) 2312–2317.
[19] W. Wang, L. Kuai, W. Cao, M. Huttula, S. Ollikkala, T. Ahopelto, A.P. Honkanen, S. Huotari, M. Yu, B. Geng, Mass-production of mesoporous $MnCo_2O_4$ spinels with manganese(IV)- and cobalt(II)-rich surfaces for superior bifunctional oxygen electrocatalysis, Angew. Chem. Int. Ed. Engl. 56 (2017) 14977–14981.
[20] Z. Guo, F. Wang, Y. Xia, J. Li, A.G. Tamirat, Y. Liu, L. Wang, Y. Wang, Y. Xia, In situ encapsulation of core–shell-structured Co@Co_3O_4 into nitrogen-doped carbon polyhedra as a bifunctional catalyst for rechargeable Zn–air batteries, J. Mater. Chem. A 6 (2018) 1443–1453.
[21] F. Dionigi, P. Strasser, NiFe-based (oxy)hydroxide catalysts for oxygen evolution reaction in non-acidic electrolytes, Adv. Energy Mater. 6 (2016) 1600621.
[22] S.T. Oyama, Preparation of Solid Catalysts, in: G. Ertl, H. Knozinger (Eds.), J. Weitkamp, Wiley-VCH, Verlag GmbH, 1999.
[23] R.B. Levy, M. Boudart, Platinum-like behavior of tungsten carbide in surface catalysis, Science 181 (1973) 547–549.
[24] K. Xu, P. Chen, X. Li, Y. Tong, H. Ding, X. Wu, W. Chu, Z. Peng, C. Wu, Y. Xie, Metallic nickel nitride nanosheets realizing enhanced electrochemical water oxidation, J. Am. Chem. Soc. 137 (2015) 4119–4125.
[25] G. He, M. Qiao, W. Li, Y. Lu, T. Zhao, R. Zou, B. Li, J.A. Darr, J. Hu, M.M. Titirici, I.P. Parkin, S. N-Co-Doped Graphene-Nickel, Cobalt sulfide aerogel: improved energy storage and electrocatalytic performance, Adv. Sci. 4 (2017) 1600214.
[26] C. Wang, H. Zhang, J. Wang, Z. Zhao, J. Wang, Y. Zhang, M. Cheng, H. Zhao, J. Wang, Atomic Fe embedded in carbon nanoshells–graphene nanomeshes with enhanced oxygen reduction reaction performance, Chem. Mater. 29 (2017) 9915–9922.
[27] G. Fu, Z. Cui, Y. Chen, L. Xu, Y. Tang, J.B. Goodenough, Hierarchically mesoporous nickel-iron nitride as a cost-efficient and highly durable electrocatalyst for Zn-air battery, Nano Energy 39 (2017) 77–85.
[28] Z. Weng, W. Liu, L.C. Yin, R. Fang, M. Li, E.I. Altman, Q. Fan, F. Li, H.M. Cheng, H. Wang, Metal/oxide interface nanostructures generated by surface segregation for electrocatalysis, Nano Lett. 15 (2015) 7704–7710.
[29] I.M. Neklyudov, A.N. Morozov, Formation and decay kinetics of nickel nitrides resulting from nitrogen ion implantation. The nickel–nitrogen phase diagram, Phys. B: Condens. Matter 350 (2004) 325–337.
[30] A. Leineweber, H. Jacobs, S. Hull, Ordering of nitrogen in nickel nitride Ni_3N determined by neutron diffraction, Inorg. Chem. 40 (2001) 5818–5822.
[31] C.M. Fang, M.H.F. Sluiter, M.A. van Huis, H.W. Zandbergen, Structure and magnetic properties of nickel nitride thin film synthesized by plasma-based ion implantation, Phys. Rev. B 86 (2012) 134114.
[32] D. Vempaire, S. Miraglia, A. Sulpice, L. Ortega, E.K. Hlil, D. Fruchart, J. Pelletier, Structure and magnetic properties of nickel nitride thin film synthesized by plasma-based ion implantation, J. Magn. Magn. Mater. 272- 276 (2004) E843–E844.
[33] D. Vempaire, S. Miraglia, J. Pelletier, D. Fruchart, E.K. Hlil, L. Ortega, A. Sulpice, F. Fettar, Structural and magnetic properties of Ni_3N synthesized by multidipolar microwave plasma-assisted reactive sputtering, J. Alloy. Compd. 480 (2009) 225–229.
[34] W. Tang, E. Sanville, G. Henkelman, A grid-based Bader analysis algorithm without lattice bias, J. Phys. : Condens. Matter 21 (2009) 084204.
[35] E. Sanville, S.D. Kenny, R. Smith, G. Henkelman, Improved grid-based algorithm for Bader charge allocation, J. Comput. Chem. 28 (2007) 899–908.
[36] Z. Yang, M. Xu, Y. Liu, F. He, F. Gao, Y. Su, H. Wei, Y. Zhang, Nitrogen-doped, carbon-rich, highly photoluminescent carbon dots from ammonium citrate, Nanoscale 6 (2014) 1890–1895.
[37] C. Hu, L. Dai, Multifunctional carbon-based metal-free electrocatalysts for simultaneous oxygen reduction, oxygen evolution, and hydrogen evolution, Adv. Mater. 29 (2017) 1604942.
[38] K. Gong, F. Du, Z. Xia, M. Durstock, L. Dai, Nitrogen-doped carbon nanotube arrays with high electrocatalytic activity for oxygen reduction, Science 323 (2009) 760–764.
[39] Y. Yu, W. Gao, Z. Shen, Q. Zheng, H. Wu, X. Wang, W. Song, K. Ding, A novel Ni_3N/graphene nanocomposite as supercapacitor electrode material with high capacitance and energy density, J. Mater. Chem. A 3 (2015) 16633–16641.
[40] J. Yang, G.X. Zhu, Y.J. Liu, J.X. Xia, Z.Y. Ji, X.P. Shen, S.K. Wu, Fe_3O_4-decorated Co_9S_8 nanoparticles in situ grown on reduced graphene oxide: a new and efficient electrocatalyst for oxygen evolution reaction, Adv. Funct. Mater. 26 (2016) 4712–4721.
[41] X. Han, C. Yu, S. Zhou, C. Zhao, H. Huang, J. Yang, Z. Liu, J. Zhao, J. Qiu, Ultrasensitive iron-triggered nanosized Fe–CoOOH integrated with graphene for highly efficient oxygen evolution, Adv. Energy Mater. 7 (2017) 1602148.
[42] H.F. Wang, C. Tang, B. Wang, B.Q. Li, Q. Zhang, Bifunctional transition metal hydroxysulfides: room-temperature sulfurization and their applications in Zn–air batteries, Adv. Mater. 29 (2017) 1702327.
[43] A.M. Chaparro, R. Benítez, L. Gubler, G.G. Scherer, L. Daza, Study of membrane electrode assemblies for PEMFC, with cathodes prepared by the electrospray method, J. Power Sources 169 (2007) 77–84.
[44] X. Zheng, B. Zhang, P. De Luna, Y. Liang, R. Comin, O. Voznyy, L. Han, F.P. García de Arquer, M. Liu, C.T. Dinh, T. Regier, J.J. Dynes, S. He, H.L. Xin, H. Peng, D. Prendergast, X. Du, E.H. Sargent, Theory-driven design of high-valence metal sites for water oxidation confirmed using in situ soft X-ray absorption, Nat. Chem. 10 (2018) 149–154.
[45] B. Zhang, X. Zheng, O. Voznyy, R. Comin, M. Bajdich, M. García-Melchor, L. Han, J. Xu, M. Liu, L. Zheng, F.P. García de Arquer, C.T. Dinh, F. Fan, M. Yuan, E. Yassitepe, N. Chen, T. Regier, P. Liu, Y. Li, P. De Luna, A. Janmohamed, H.L. Xin, H. Yang, A. Vojvodic, E.H. Sargent, Homogeneously dispersed multimetal oxygen-evolving catalysts, Science 352 (2016) 333–337.
[46] S. Jin, Are metal chalcogenides, nitrides, and phosphides oxygen evolution catalysts or bifunctional catalysts?, ACS Energy Lett. 2 (2017) 1937.
[47] Y. Zhang, B. Ouyang, J. Xu, G. Jia, S. Chen, R.S. Rawat, H.J. Fan, Rapid synthesis of cobalt nitride nanowires: highly efficient and low-cost catalysts for oxygen evolution, Angew. Chem. Int. Ed. 55 (2016) 8670–8674.
[48] J. Masa, P. Weide, D. Peeters, I. Sinev, W. Xia, Z. Sun, C. Somsen, M. Muhler, W. Schuhmann, Amorphous cobalt boride (Co_2B) as a highly efficient nonprecious catalyst for electrochemical water splitting: oxygen and hydrogen evolution, Adv. Energy Mater. 6 (2016) 1502313.